Critical magnetic field for lifting the degeneracy of monochiral domain walls with strong interlayer antiferromagnetic coupling

Tie Zhou,[1] Xuejie Xie,[1] Xiaonan Zhao,[1] Yanan Dong,[1] Jing Wang,[1] Weibin Chen,[1,2] Qikun Huang,[1] Qunwen Leng,[2] Lihui Bai,[1] Yanxue Chen,[1] Shishen Yan ![ORCID],[1,3,*] and Yufeng Tian[1,†]

[1]*School of Physics, State Key Laboratory of Crystal Materials, Shandong University, Jinan 250100, People's Republic of China*
[2]*Beihang University, Beihang Goertek Joint Microelectronics Institute, Qingdao Research Institute, Qingdao 266101, People's Republic of China*
[3]*School of Physics & Electronic Engineering, Kashgar University, Kashi 844006, People's Republic of China*

The addition of spatial inversion asymmetry and significant spin-orbit coupling to synthetic antiferromagnets (SAFs) has led to a lot of fundamental discoveries and technological applications. Here, we experimentally demonstrate that the critical magnetic field for breaking the degeneracy of monochiral domain walls (DWs) to realize the spin-orbit torque (SOT)-induced magnetization switching can be varied in a wide range from field free to 3000 Oe in perpendicularly magnetized CoPt/Ru/CoPt SAFs with strong interlayer antiferromagnetic coupling, which strongly depends on the interfacial Dzyaloshinsky-Moriya interaction (DMI) and SOT at the bottom and top interfaces with multiple inversion asymmetries. Our DW dynamical calculations further reveal that the field-free magnetization switching is caused by SOT-induced left-handed chiral Néel DW displacement under the condition that the interfacial DMI of the upper magnetic layer has a significantly smaller value than that of the lower magnetic layer. These findings provide key insights for understanding the role of SOT and DMI in magnetization switching of magnetically coupled chiral systems and pave the way to practical applications of SAFs.

I. INTRODUCTION

The combination of spatial inversion asymmetry and significant spin-orbit coupling in synthetic antiferromagnets (SAFs) based on ferromagnet/spacer/ferromagnet multilayered stacks with antiparallel magnetizations has led to a lot of fundamental discoveries and technological applications [1–19]. The perpendicularly magnetized SAFs with strong interlayer antiferromagnetic coupling (IAC) are expected to be very promising for practical applications in nonvolatile memory and spin-logic devices due to good thermal stability, fast magnetic dynamics, and highly efficient spin-orbit torque (SOT) switching [5–7,10,11]. In addition to the well-known oscillatory interlayer exchange coupling and giant magnetoresistance [12,13], recent emerging findings in SAFs include SOT-induced magnetization switching [5–7,17–19], large domain wall (DW) velocity [2], magnetic bilayer skyrmions without the skyrmion Hall effect [14], artificial spin ice [15], and a chiral magnetic DW serving as a spin-wave polarizer and retarder [16]. Among all these findings it is worthy to mention that, though the field-free magnetization switching has been realized recently in SAFs with very weak IAC [17–19], a large in-plane external magnetic field of 500 to 4000 Oe is still needed in SAFs with strong IAC to obtain deterministic perpendicular magnetization switching by SOT

[5–7], which seriously limits the practical applications of SAFs. It is worth mentioning that strong IAC in SAFs is necessary for remaining at zero net magnetization (without a stray field) in a relatively large external magnetic field, enhancing the thermal stability of magnetization, keeping high resonance frequency, and locking the two magnetizations antiparallel to behave as a whole.

In principle, due to spatial inversion asymmetry and significant spin-orbit coupling at the bottom and top interfaces of SAFs, the Dzyaloshinsky-Moriya interaction (DMI) can result in monochiral DWs [2,5,7], such as two left-handed chiral DWs with up-to-down and down-to-up configurations, respectively. Without the external magnetic field and/or applied electric current, the two chiral DWs have the same static magnetic energy, i.e., degeneracy of monochiral DWs. Under the in-plane external magnetic field and/or the applied electric current, the two chiral DWs have different energy and move with different velocity, i.e., breaking the degeneracy of monochiral DWs, which can cause the perpendicular magnetization to switch [2,5,7]. Though the dynamics of monochiral DW movement can be well described by the Landau-Lifshitz-Gilbert (LLG) equation [2,20], the critical magnetic field for breaking the degeneracy of monochiral DWs to switch the perpendicular magnetization has not been given yet.

On the other hand, we wonder if the degeneracy of monochiral DWs can be broken without any external magnetic field to realize field-free perpendicular magnetization switching in SAFs with strong IAC by designing multiple inversion asymmetries. In fact, in addition to the conventional

---

*shishenyan@sdu.edu.cn
†yftian@sdu.edu.cn

out-of-plane inversion asymmetry (along the z axis), the in-plane inversion asymmetry (along the y axis) can also form at the heterojunction interface [21–25]. Moreover, the different bottom buffer layers and top capping layers in the SAF can further reduce its symmetry, which can be easily used to modulate the interfacial DMI and SOT of the bottom and top interfaces [26–29]. However, experimental and theoretical investigations on the strong coupling SAF with multiple inversion asymmetries are still lacking.

In this paper, we experimentally and theoretically demonstrate that the critical magnetic field for the SOT-induced magnetization switching can be varied in a wide range from field free to 3000 Oe in perpendicularly magnetized CoPt/Ru/CoPt SAFs with strong IAC, which strongly depends on the interfacial DMI and SOT at the bottom and top interfaces with multiple inversion asymmetries. Our DW dynamical calculations further reveal that the field-free magnetization switching is caused by SOT-induced left-handed chiral Néel DW displacement under the condition that the interfacial DMI of the upper magnetic layer (UM) has a significantly smaller value than that of the lower magnetic layer (LM).

II. SAFs WITH STRONG IAC

We prepared a series of perpendicularly magnetized CoPt/Ru/CoPt SAF with different bottom buffer layers and top capping layers to form multiple inversion asymmetries [30], i.e., substrate-Si − SiO_2/Ta2/Pt5/ [Co0.5/Pt0.3/Co0.5]/Ru0.7/[Co0.5/Pt0.3/Co0.5]/Pt1/Ta2, named as Pt-Ta-capped SAF, substrate-Si−SiO_2/Ru2/ Pt5/[Co0.5/Pt0.3/Co0.5]/Ru0.9/[Co0.5/Pt0.3/Co0.8]/Ta2/ Ru2, named as Ta-Ru-capped SAF, and substrate-Si − SiO_2/Ta2/Pt5/[Co0.5/Pt0.4/Co0.5]/Ru0.88/[Co0.4/Pt0.3 /Co0.4/Pt0.3/Co0.4]/Ta2/Pt2, named as Ta-Pt-capped SAF, where the numbers are the nominal thicknesses of each layer in units of nanometers. The Pt-Ta- and Ta-Ru-capped SAFs are prepared by normal sputtering with substrate rotation, so only the conventional out-of-plane inversion asymmetry is formed. The Ta-Pt-capped SAFs are prepared by oblique sputtering with the sputtering direction in the *y-z* plane (*z* axis perpendicular to the film plane), and in this case, both the conventional out-of-plane and in-plane inversion asymmetries can form at the bottom and top interfaces. In fact, oblique sputtering can simultaneously break crystal and structural inversion symmetry at the heterojunction interface along the two orthogonal directions of out-of-plane *z* axis and in-plane *y* axis and thus allow for the creation of two orthogonal components E_y and E_z of the inner electric field vector ($\mathbf{E} = E_y \hat{y} + E_z \hat{z}$) with inversion asymmetry. Due to the strong spin-orbit coupling at heterojunction interfaces and in the heavy metal layers, we propose that the inversion asymmetry along the *y* and *z* axes at the heterojunction interfaces can produce the SOT bias fields to break the degeneracy of up-to-down and down-to-up DW motion and lead to the deterministic switching of perpendicular magnetization with strong IAC. In these samples, the perpendicularly magnetized CoPt alloy layers formed by [Co/Pt/Co] or [Co/Pt/Co/Pt/Co] layers are separated by the intermediate Ru layer to establish the strong IAC
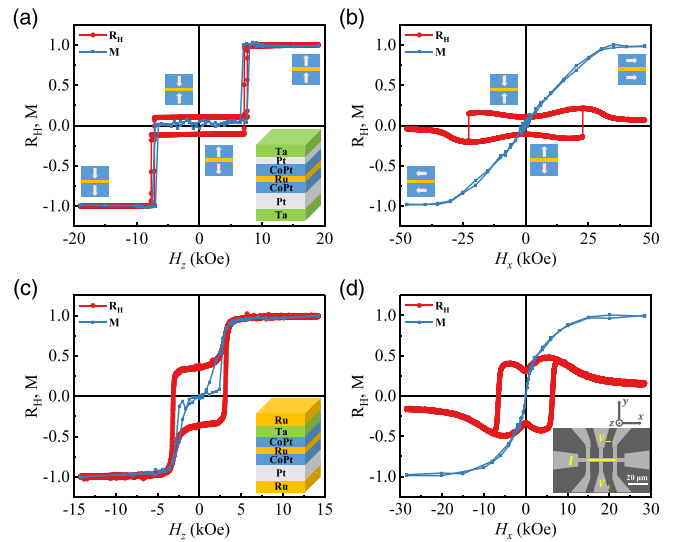
FIG. 1. Strong interlayer antiferromagnetic coupling and perpendicular magnetization measured by normalized magnetic hysteresis loops (blue) and anomalous Hall effect curves (red). (a) The external magnetic field H_z is applied out of the film plane, the easy magnetization axis of the Pt-Ta-capped synthetic antiferromagnet (SAF). The bottom inset in (a) shows the stacks of the Pt-Ta-capped SAF. (b) The external magnetic field H_x is applied in the film plane, the hard magnetization plane of the Pt-Ta-capped SAF. The schematic diagrams with arrows in (a) and (b) indicate the magnetization directions in both magnetic layers of the SAF. (c) and (d) The same measurements as (a) and (b) for the Ta-Ru-capped SAF. The bottom inset in (c) shows the stacks of the Ta-Ru-capped SAF. The bottom inset in (d) shows the structural diagram of Hall bar.

[2,5,7,13]. The different bottom buffer layers and top capping layers are used to modulate the SOT and interfacial DMI of the bottom and top interfaces [26–29], which are very important to modulate the critical magnetic field and even realize the field-free SOT-induced magnetization switching in SAFs with strong IAC. The magnetic hysteresis loops were measured with a superconducting quantum interference device. Current-induced magnetization switching by SOT was measured by applying a 0.1 s current pulse with different amplitudes to the Hall bar. A one-dimensional model of DW dynamics in SAFs is based on the LLG equation of magnetization dynamics. The stationary solutions of DW motion under applied electric current and magnetic field are described by the DW velocity and the azimuthal angle of the in-plane component of magnetization at the center of the DWs.

Figures 1(a) and 1(b) show the normalized magnetic hysteresis loops and anomalous Hall effect curves of the Pt-Ta-capped SAF, and Figs. 1(c) and 1(d) show the similar loops of the Ta-Ru-capped SAF. Strong IAC, perpendicular magnetization, and zero net magnetization at the antiferromagnetic remanent magnetization states are observed in both Pt-Ta- and Ta-Ru-capped SAFs. In Fig. 1(a), although the remanent magnetization of the SAF is zero, the remanent Hall resistance is nonzero due to different shunting resistance and interfacial spin-orbit coupling in the bottom buffer layers and top capping layers [7]. Therefore, as the external mag-

netic field reduces from the positive magnetization saturation to zero, one antiferromagnetic remanent magnetization state ($M_L \uparrow$ in the LM, $M_U \downarrow$ in the UM), as shown in Fig. 1(a), is obtained which can be measured by the positive remanent Hall resistance R_H. On the other hand, as the external magnetic field reduces from the negative magnetization saturation to zero, another antiferromagnetic remanent magnetization state ($M_L \downarrow$ in the LM, $M_U \uparrow$ in the UM) can be obtained and measured by the negative remanent Hall resistance R_H. This means that we can write two different antiferromagnetic remanent magnetization states by using two large magnetic fields (the positive/negative magnetization saturation fields along the z axis) and read them by the anomalous Hall effect for the application in nonvolatile memory. However, Fig. 1 indicates that all these perpendicularly magnetized SAFs with strong IAC need a large magnetic field to switch (write) the two antiferromagnetic remanent magnetization states, which should be removed for practical applications in nonvolatile memory by the field-free SOT-induced magnetization switching in SAFs. A quantitative estimation of the perpendicular magnetic anisotropy and strong IAC can be found in Supplemental Material I [31].

III. PERPENDICULAR MAGNETIZATION SWITCHING BY SOT

Figure 2(a) shows the schematic diagram of an antiferromagnetically coupled Néel-type DW with the left-handed chirality and the effective magnetic fields acting on the center of DWs in SAFs. The DW ($\uparrow\leftarrow\downarrow$) in the LM and the DW ($\downarrow\rightarrow\uparrow$) in the UM, which strongly couple together and move as a whole in SAFs, are referred to as DW1, and the DW ($\downarrow\rightarrow\uparrow$) in the LM and the DW ($\uparrow\leftarrow\downarrow$) in the UM as a whole are referred to as DW2. The magnetization switching is caused by the relative movement between DW1 and DW2 under all the effective magnetic fields in SAFs [2,5]. In all our SAFs, the bottom buffer layer of Pt5 heavy metal is significantly thicker than the top capping layer of heavy metal Ta2, Pt1/Ta2, or Ta2/Pt2, so the chirality of antiferromagnetically coupled Néel DWs and the effective SOT acting on DW1 and DW2 are mainly determined by the bottom Pt layer, and the sign of antiferromagnetic remanent Hall resistance R_H is also determined by the LM. The detail of the DMI effective magnetic field in SAFs is shown in Supplemental Material II [31]. The DMI effective fields at the bottom interface are measured as 1300 Oe for Pt-Ta-capped SAF and 3600 Oe for the Ta-Ru-capped SAF.

Figure 2(b) shows the electric-current-induced perpendicular magnetization switching of the Pt-Ta-capped SAF at various in-plane magnetic fields H_x. The Pt-Ta-capped SAF shows a low magnetic field magnetization switching at an in-plane external magnetic field as low as 70 Oe, which is denoted by the shadow loops. As H_x increases to 2400 Oe, the magnetization switching disappears, and it appears again as H_x continues to increase >2400 Oe. This phenomenon can be well explained by the relative movement between DW1 and DW2, i.e., no deterministic magnetization switching can be observed at $H_x = 2400$ Oe because DW1 and DW2 move at the same velocity [2,5]. By contrast, the Ta-Ru-capped SAF in Fig. 2(c) only shows significant magnetization switching
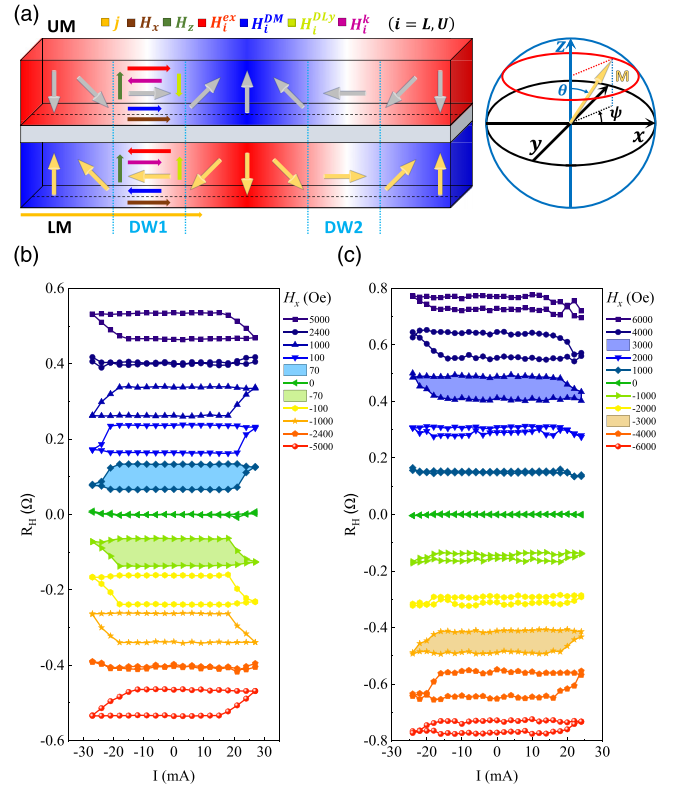
FIG. 2. The schematic diagram of antiferromagnetically coupled Néel domain wall (DW) and current-induced perpendicular magnetization switching by spin-orbit torque (SOT) in a synthetic antiferromagnet (SAF). (a) The schematic diagram of antiferromagnetically coupled Néel DW with left-handed chirality in the SAF. The antiferromagnetically coupled DW ($\uparrow\leftarrow\downarrow$) in the lower magnetic layer (LM) and DW ($\downarrow\rightarrow\uparrow$) in the upper magnetic layer (UM) as a whole are referred to as DW1, and the DW ($\downarrow\rightarrow\uparrow$) in the LM and DW ($\uparrow\leftarrow\downarrow$) in the UM as a whole are referred to as DW2 for the SAF. The right side of (a) gives a schematic diagram of coordinate systems, which illustrates the directions of the x, y, and z axes (Cartesian coordinates), and the magnetization vector $\mathbf{M} = M(\theta, \psi)$ described by the polar angle θ and azimuth angle ψ (spherical coordinates). (b) The Pt-Ta-capped SAF shows a low magnetic field magnetization switching at an in-plane external magnetic field as low as 70 Oe, which is denoted by the shadow loops. (c) The Ta-Ru-capped SAF only shows significant magnetization switching at a large magnetic field >3000 Oe, which is denoted by the shadow loops.

at a large magnetic field of 3000 Oe, which is also denoted by the shadow loops. The magnetization switching is always clockwise, from positive Hall resistance switching to negative Hall resistance at positive current I and field H_x.

In the shadow loops of Fig. 2(b), the critical current for magnetization switching is $I_{\mathrm{crit}} = 23.0$ mA, which can be used to estimate the averaged current density. If the current only passes through the Pt layers in the SAF, the maximum value of current density $j_{\max}$ can be obtained. If the current passes uniformly in the SAF, the minimum value of current density $j_{\min}$ can be obtained. Here, for the Pt-Ta-capped SAF, $j_{\max} = 6.97 \times 10^7$ A cm^{-2} and $j_{\min} = 3.46 \times 10^7$ A cm^{-2} are obtained. For the Ta-Ru-capped SAF, it can be

obtained that $I_{crit} = 20.8$ mA, $j_{max} = 7.43 \times 10^7$ A cm^{-2}, and $j_{min} = 2.81 \times 10^7$ A cm^{-2} from the shadow loops in Fig. 2(c). It is easy to find that the practical current density in the SAF should be between j_{min} and j_{max} despite its nonuniformity. The detail of the electric-current-induced SOT effective magnetic field in SAFs is shown in Supplemental Material III [31].

IV. CRITICAL MAGNETIC FIELD FOR MAGNETIZATION SWITCHING

Now we turn to quantitatively study the DW dynamics to reveal the physical mechanisms of magnetization switching. We consider all effective magnetic fields acting on the DWs since the chiral DW movement plays a key role in SOT-induced magnetization switching [2,5–7,10,11]. In general, we consider the LLG equation of each magnetic layer in SAFs, which can include the magnetization precession, magnetization damping, adiabatic and nonadiabatic spin-transfer torques (STT), and all fieldlike and dampinglike SOT caused by spin polarization in $\hat{x}$, $\hat{y}$, and $\hat{z}$ directions of the spin current [2,20]:

$$\frac{\partial \mathbf{M}}{\partial t} = -\gamma \mathbf{M} \times \mathbf{H} + \frac{\alpha}{M} \mathbf{M} \times \frac{\partial \mathbf{M}}{\partial t} - \frac{u}{M^2} \mathbf{M} \times \left(\mathbf{M} \times \frac{\partial \mathbf{M}}{\partial x} \right)$$

$$- \frac{\beta u}{M} \mathbf{M} \times \frac{\partial \mathbf{M}}{\partial x} + \gamma H^{FLx} \mathbf{M} \times \hat{x} + \frac{\gamma H^{DLx}}{M} \mathbf{M} \times (\mathbf{M} \times \hat{x})$$

$$+ \gamma H^{FLy} \mathbf{M} \times \hat{y} + \frac{\gamma H^{DLy}}{M} \mathbf{M} \times (\mathbf{M} \times \hat{y})$$

$$+ \gamma H^{FLz} \mathbf{M} \times \hat{z} + \frac{\gamma H^{DLz}}{M} \mathbf{M} \times (\mathbf{M} \times \hat{z}). \quad (1)$$

The item of $-\gamma \mathbf{M} \times \mathbf{H}$ is the precession of magnetic moment $\mathbf{M}$ under the total static effective magnetic field $\mathbf{H}$, where $\gamma = 1.76086 \times 10^7$ Oe^{-1} s^{-1} is the gyromagnetic ratio for an isolated electron. The total static effective magnetic field $\mathbf{H}$, which acts on DW1 and DW2, includes the DMI effective field $\mathbf{H}_i^{DM}$ (the subscript $i = L$, U for the LM and the UM, respectively), IAC field $\mathbf{H}_i^{ex}$, in-plane demagnetization field $\mathbf{H}_i^k$ of the DWs, and the external magnetic field such as $\mathbf{H}_x$ or $\mathbf{H}_z$. By the way, the static inner exchange interaction effective field and static perpendicular anisotropy effective field also take role through the DW width in the one-dimensional DW model. The item of $\frac{\alpha}{M} \mathbf{M} \times \frac{\partial \mathbf{M}}{\partial t}$ is the damping of magnetic moment $\mathbf{M}$, where α is the damping factor. The effects of STT are parameterized by u, and the items of $-\frac{u}{M^2} \mathbf{M} \times (\mathbf{M} \times \frac{\partial \mathbf{M}}{\partial x})$ and $-\frac{\beta u}{M} \mathbf{M} \times \frac{\partial \mathbf{M}}{\partial x}$ are adiabatic and nonadiabatic STT, where β is the nonadiabatic STT coefficient [32,33]. The adiabatic and nonadiabatic STT items can be neglected in our SAFs. The item of $\gamma H^{FLy} \mathbf{M} \times \hat{y}$ can serve as the fieldlike SOT caused by the spin Hall effect, where $\hat{y}$ is the spin-polarization unit vector in the y axis direction of spin current flowing along the z axis direction. The item of $\frac{\gamma H^{DLy}}{M} \mathbf{M} \times (\mathbf{M} \times \hat{y})$ can serve as the dampinglike SOT caused by the spin Hall effect. In fact, since the spin current in our SAF has no spin polarization in the $\hat{x}$ direction, we set the two parameters $H^{FLx} = H^{DLx} = 0$. Considering that the SOT fields along the z direction dominate the DW motion rather than the SOT fields in the x-y plane, we can also set $H^{FLy} = H^{DLz} = 0$ in calculations. Thus, in our
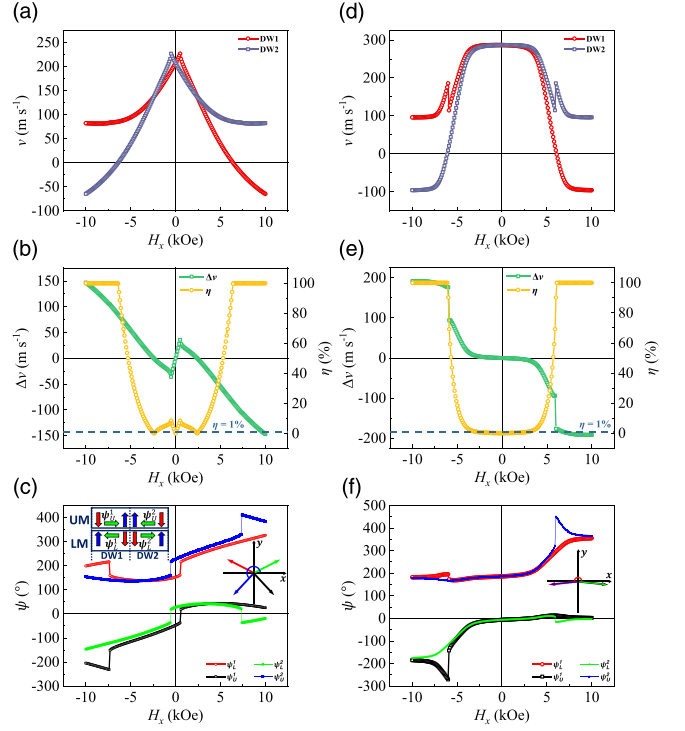
FIG. 3. Theoretical calculations of domain wall (DW) velocity and azimuth angle ψ in a synthetic antiferromagnet (SAF) as a function of applied magnetic field H_x by using experimental parameters. (a) The calculated velocity of DW1 (red) and DW2 (blue) in the Pt-Ta-capped SAF. (b) The DW velocity difference Δv (green) and the relative ratio of velocity difference η (yellow) between DW1 and DW2 in the Pt-Ta-capped SAF. The dash line shows $\eta = 1\%$, at which the critical switching magnetic field (H^{crit}) is defined for deterministic magnetization switching in experiments. (c) The calculated azimuth angles (ψ_L^1, ψ_U^1) of DW1 and (ψ_L^2, ψ_U^2) of DW2 at different H_x in the Pt-Ta-capped SAF. The inset on the right shows the DW configurations of DW1 and DW2 at $H_x = 0$. (d)–(f) The corresponding calculations for the Ta-Ru-capped SAF as in (a)–(c).

case, we only consider the SOT effective fields along the z axis, i.e., the fieldlike SOT effective field $H^{FLz} \neq 0$ and the dampinglike SOT effective field $H^{DLy} \neq 0$, without losing the basic physics in Eq. (1).

Here, we applied the above LLG equation to the one-dimensional DW model to study the DW dynamics quantitatively [2,20,34] (see Supplemental Material IV and V and Fig. S5 [31]). The physical parameters used in the one-dimensional DW calculations are mainly based on the experimental values, which are shown in Table S1 in the Supplemental Material [31]. Figure 3(a) shows the velocity of DW1 and DW2 as a function of the external field H_x for the Pt-Ta-capped SAF, which is calculated by Eqs. (33)–(39) in Supplemental Material IV [31]. As shown in Table S1 in the Supplemental Material [31], the DMI effective field $H_L^{DM} = -1625$ Oe and $H_U^{DM} = 500$ Oe are used for DW1 of the Pt-Ta-capped SAF. The dampinglike SOT effective field $H_L^{DLy} = 200$ Oe (corresponding to current density $j_L = 6.84 \times 10^7$ A cm^{-2} in the bottom Pt layer, which is between experimental j_{min} and

$j_{\max}$) and $H_U^{DLy} = 100$ Oe are used in calculations for DW1. This scenario of effective magnetic fields is appropriate for SAFs with the conventional out-of-plane inversion asymmetry (along the z axis). DW1 and DW2 have the same velocities at $H_x = 0$ and $H_x = \pm 2400$ Oe. At these three magnetic fields, the magnetization switching cannot occur, which is in good agreement with the experimental observation in Fig. 2(b).

According to the one-dimensional DW model, magnetization switching can occur as soon as DW1 and DW2 have different velocities for SAFs with multiple magnetic domains. The prerequisite for the DW model is the existence of the multiple magnetic domains and corresponding DWs, which are usually pinned by the defects or nonuniformity in the magnetic layers. The very small reversed magnetic domains are usually first formed before the magnetization switching at the defects or the edges of the samples due to the combination of the Joule heat, SOT, and reversed external magnetic field. However, even though DW1 and DW2 have depinned from the defects or the edges, they still cannot cause the deterministic magnetization switching if they have the same DW velocity. Comparing Figs. 2(b) and 3(a), there is an obvious correlation between the experimental magnetization switching and the theoretical velocity difference between DW1 and DW2. Therefore, we define the velocity difference between DW1 and DW2 as $\Delta v = v_{DW1} - v_{DW2}$ and the relative ratio of velocity difference as $\eta = \frac{|v_{DW1} - v_{DW2}|}{|v_{DW1}| + |v_{DW2}|}$, which are shown in Fig. 3(b). Here, the critical magnetic field H^{crit} for the SOT-induced significant magnetization switching can be defined as the minimum magnetic field that satisfies $\eta \geqslant 1\%$.

Combining Figs. 3(b) and 2(b), we can know that, in the positive magnetic field range with $\Delta v > 0$ and $\eta \geqslant 1\%$, the magnetization switching at positive current I and magnetic field $H_x < 2400$ Oe in Fig. 2(b) is due to DW1 movement along the $+\hat{x}$ axis dominating over DW2 movement in Fig. 3(b), showing anticlockwise switching from negative to positive Hall resistance in Fig. 2(b). In Fig. 3(b), the theoretical critical magnetic field $H^{crit} = 70$ Oe for the Pt-Ta-capped SAF is in excellent agreement with the applied magnetic field $H_x = 70$ Oe, at which significant magnetization switching is observed, as shown in Fig. 2(b). On the other hand, in the positive magnetic field range with $\Delta v < 0$ and $\eta \geqslant 1\%$ in Fig. 3(b), the magnetization switching at positive current I and magnetic field $H_x > 2400$ Oe in Fig. 2(b) is due to DW2 movement along the $+\hat{x}$ axis dominating over DW1 movement in Fig. 3(b), showing clockwise switching from positive to negative Hall resistance in Fig. 2(b).

Figure 3(c) shows the calculated azimuth angles (ψ_L^1, ψ_U^1) of DW1 and (ψ_L^2, ψ_U^2) of DW2 at different H_x, and the inset on the right shows the DW configurations of DW1 and DW2 at $H_x = 0$ ($\psi_L^1 = 153°$, $\psi_U^1 = -47°$, $\psi_L^2 = 27°$, and $\psi_U^2 = 227°$). The azimuth angles (ψ_L^1, ψ_U^1) of DW1 are not symmetrical about the y axis at $H_x = 0$, which means that DW1 has the net magnetization component along the $-\hat{x}$ axis direction. For the same reason, DW2 has the net magnetization component along the $+\hat{x}$ axis direction. In this case, a small external magnetic field H_x along the x axis can break the symmetry of DW1 and DW2 about the y axis and

makes them have different DW velocities to switch the magnetization.

Similar calculations are done for the Ta-Ru-capped SAF using $H_L^{DM} = -3600$ Oe, $H_U^{DM} = 3600$ Oe, $H_L^{DLy} = 100$ Oe (corresponding to current density $j_L = 3.50 \times 10^7$ A cm^{-2} in the bottom Pt layer) and $H_U^{DLy} = 50$ Oe, which are shown in Figs. 3(d)–3(f). In this case, we find that DW1 and DW2 have the same velocities $\eta = 0$ at $H_x = 0$ and $\eta = 1\%$ at $H_x = 3000$ Oe. This means that a large critical magnetic field $H^{crit} = 3000$ Oe is needed for the magnetization switching of the Ta-Ru-capped SAF, which is well in agreement with the experimental observation in Fig. 2(c). Moreover, the magnetization switching at positive current I and magnetic field $H_x > 3000$ Oe in Fig. 2(c) is due to DW2 movement along the $+\hat{x}$ axis dominating over DW1 movement in the positive magnetic field range with $\Delta v < 0$ and $\eta \geqslant 1\%$ in Fig. 3(e), showing clockwise switching from positive to negative Hall resistance in Fig. 2(c).

Figure 3(f) shows the calculated azimuth angles (ψ_L^1, ψ_U^1) of DW1 and (ψ_L^2, ψ_U^2) of DW2 at different H_x. It is clear that the azimuth angles (ψ_L^1, ψ_U^1) of DW1 are symmetrical about the y axis at $H_x = 0$ ($\psi_L^1 = 186°$, $\psi_U^1 = -6°$, $\psi_L^2 = -6°$, and $\psi_U^2 = 186°$), which means that DW1 has no net magnetization component along the x axis. For the same reason, DW2 also has no net magnetization component along the x axis. In this case, a large external magnetic field H_x along the x axis is needed to break the symmetry of DW1 and DW2 about the y axis to switch the magnetization.

Since the critical magnetic field H^{crit} is key for magnetization switching, it is necessary to study its dependence on other physical parameters, such as H_L^{DM}, H_U^{DM}, $-J^{ex}$, H^k, and j. Figure 4(a) shows the contour plot of H^{crit} vs H_L^{DM} and H_U^{DM} of DW1. Since H_L^{DM} is negative and H_U^{DM} is positive (along the x axis) for DW1 in our SAF samples, as shown in Fig. 2(a), the fourth quadrant of the contour plot in Fig. 4(a) corresponds to our experimental case. This quadrant of the plot shows the remarkable characteristic that H^{crit} increases as the strength of H_L^{DM} and H_U^{DM} simultaneously increases within the diagonal region, and H^{crit} is mainly determined by the weaker one of H_L^{DM} and H_U^{DM}. In practical application of SAFs, we want H^{crit} as small as possible, preferably zero. Now the characteristic of the contour plot of H^{crit} provides an important reference for us to achieve this goal that a low critical field and even field-free magnetization switching can be obtained by designing a weak DMI at either the LM or the UM despite the large IAC and large DMI in the other magnetic layer.

Figure 4(b) further shows H^{crit} as a function of $|H^{DM}|$, where $|H^{DM}| = -H_L^{DM} = H_U^{DM} > 0$ varies along the diagonal in the fourth quadrant. When $|H^{DM}|$ is < 1000 Oe, H^{crit} is zero, which predicts a field-free magnetization switching. When $|H^{DM}|$ is > 1000 Oe, H^{crit} increases nearly linearly with $|H^{DM}|$.

Now we turn to the first quadrant of Fig. 4(a), where $H_L^{DM} > 0$ and $H_U^{DM} > 0$ in DW1 mean the right-handed Néel DW ($\uparrow \rightarrow \downarrow$) in the LM and the left-handed Néel DW ($\downarrow \rightarrow \uparrow$) in the UM. In the first quadrant, the critical field H^{crit} is quite small in most regions except a narrow region above the diagonal. Very similar results are obtained in the third quadrant of Fig. 4(a), which is the inversion of the first quad-
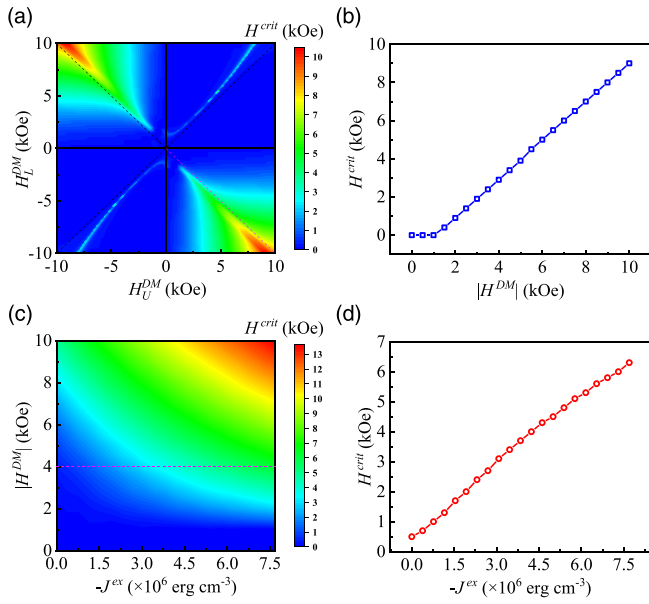
FIG. 4. The dependence of critical switching magnetic field H^{crit} on H_L^{DM}, H_U^{DM}, and $-J^{ex}$. (a) The contour plot of H^{crit} vs H_L^{DM} and H_U^{DM}, where the other physical parameters are from the values of the Pt-Ta-capped synthetic antiferromagnet (SAF). (b) The dependence of H^{crit} on $|H^{DM}|$, which corresponds to the dashed line in the fourth quadrant of (a) with $|H^{DM}| = -H_L^{DM} = H_U^{DM}$ for DW1. (c) The contour plot of H^{crit} vs $|H^{DM}|$ and $-J^{ex}$, where $|H^{DM}| = -H_L^{DM} = H_U^{DM}$ for DW1. (d) The dependence of H^{crit} on $-J^{ex}$ for the fixed $|H^{DM}| = 4000$ Oe, which corresponds to the dashed line in (c).

rant. Obviously, the critical field H^{crit} in the second quadrant, where $H_L^{DM} > 0$ and $H_U^{DM} < 0$ in DW1 mean the right-handed Néel DW ($\uparrow \rightarrow \downarrow$) in the LM and the right-handed Néel DW ($\downarrow \leftarrow \uparrow$) in the UM, is also the inversion of the fourth quadrant.

The contour plot of H^{crit} vs $|H^{DM}|$ and $-J^{ex}$ is shown in Fig. 4(c), where $|H^{DM}| = -H_L^{DM} = H_U^{DM} > 0$ for DW1. When $|H^{DM}|$ is fixed at 4000 Oe, represented by the horizontal dash line in Fig. 4(c), the variation of H^{crit} with $-J^{ex}$ is given in Fig. 4(d). Figures 4(c) and 4(d) indicate that H^{crit} increases with both $|H^{DM}|$ and $-J^{ex}$. We also calculated H^{crit} as a function of DW demagnetization field H^k and current density j (see Fig. S6 in Supplemental Material V [31]), indicating that the increase of H^k and j is helpful to reduce H^{crit}. By the way, for the calculations in Figs. 3 and 4, the current density applied in our SAFs is so small that its STT effect on DW dynamics is neglected (see Fig. S7 in Supplemental Material V [31]).

V. FIELD-FREE SOT-INDUCED MAGNETIZATION SWITCHING

So far, we have experimentally achieved a significant decrease of the critical switching field H^{crit} from 3000 to 70 Oe mainly by designing both DMI effective fields H_L^{DM} and H_U^{DM} in SAFs. Although a few values of H_L^{DM} and H_U^{DM} can make the $H^{crit} = 0$ in theory, as shown in Fig. 4 and Fig. S6 in Supplemental Material V [31], it is not easy to acquire these H_L^{DM} and H_U^{DM} accurately in experiments. Therefore, we further introduce the oblique sputtering to assist the realization
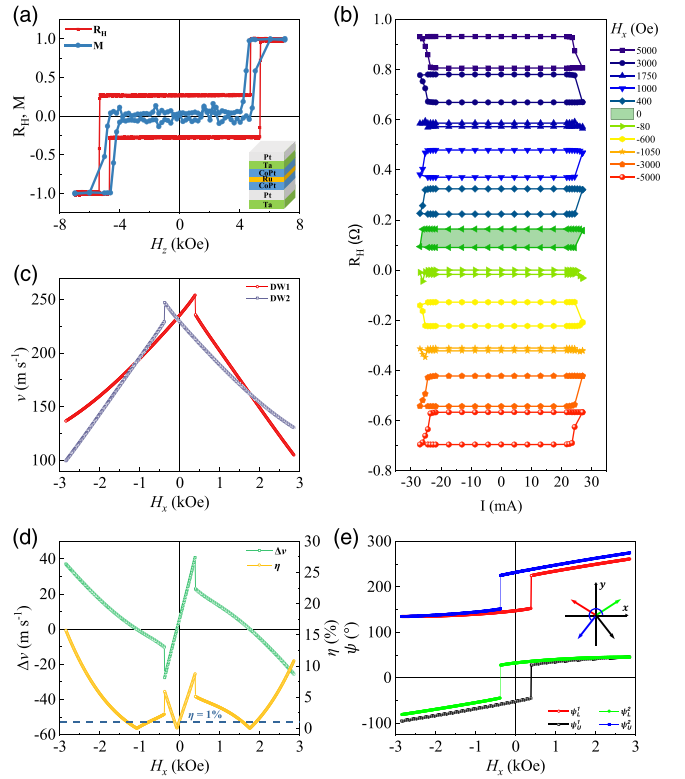
FIG. 5. Field-free spin-orbit torque (SOT) switching in an oblique sputtering synthetic antiferromagnet (SAF). (a) Normalized magnetic hysteresis loop (blue) and anomalous Hall effect curve (red) measured by out-of-plane magnetic field H_z. The bottom inset in (a) shows the stacks of the oblique sputtering SAF. (b) The oblique sputtering SAF shows a field-free magnetization switching at $H_x = 0$, which is denoted by the shadow loop. (c) The calculated velocity of DW1 (red) and DW2 (blue) in oblique sputtering SAF. (d) The domain wall (DW) velocity difference Δv (green) and the relative ratio of velocity difference η (yellow) between DW1 and DW2 in the oblique sputtering SAF. (e) The calculated azimuth angles (ψ_L^1, ψ_U^1) of DW1 and (ψ_L^2, ψ_U^2) of DW2 as a function of H_x in oblique sputtering SAF. The inset shows the DW configurations of DW1 and DW2 at $H_x = 0$.

of field-free magnetization switching in SAFs by modulating the SOT effective fields. In addition to the conventional inversion asymmetry out of the plane (along the z axis), the oblique sputtering in the y-z plane will break the space inversion symmetry in the y direction, resulting in an additional y-direction electric field $\mathbf{E}_y = E_y \hat{y}$ with inversion asymmetry. Due to the Rashba-like spin-orbit coupling, the current in the x-axis direction of the oblique sputtering SAFs can generate an additional fieldlike SOT effective field $\mathbf{H}_i^{FLz}$ (along the z axis) acting on the LM and the UM. As a result, two magnetic fields $\mathbf{H}_L^{FLz}$ and $\mathbf{H}_U^{FLz}$ should be added to the LM and the UM for the oblique sputtering SAFs. The detailed analysis of the additional fieldlike SOT effective field $\mathbf{H}_i^{FLz}$ can be found in Supplemental Material IV [31].

Figure 5(a) shows the out-of-plane magnetic hysteresis loop and anomalous Hall effect curve of the Ta-Pt-capped oblique sputtering SAF. Like the Pt-Ta- and Ta-Ru-capped

SAFs, the Ta-Pt-capped oblique sputtering SAF has strong IAC and perpendicular magnetization as well as zero net magnetization and nonzero Hall resistance at the remanent magnetization states. By fitting the magnetic hysteresis loop, the saturation magnetization $M = 702$ emu cm^{-3} (experimental value), perpendicular magnetic anisotropy $K^p = 2.817 \times 10^6$ erg cm^{-3}, and interlayer antiferromagnetic exchange coupling strength $J^{ex} = -2.189 \times 10^6$ erg cm^{-3} (or $J^{ex} = -0.3503$ erg cm^{-2}) are obtained for the oblique sputtering SAFs. The electric-current-induced magnetization switching of the SAFs is shown in Fig. 5(b). It is remarkable that field-free perpendicular magnetization switching occurs at $H_x = 0$, which is denoted by the shadow loop. As H_x varies from 5000 to -5000 Oe, there are three values of $H_x = 1750$, -80, and -1050 Oe at which the magnetization switching disappears. When H_x crosses these three fields, the magnetization switching direction (clockwise or anticlockwise) changes. In Fig. 5(b), we can obtain $I_{crit} = 27.5$ mA, $j_{max} = 6.88 \times 10^7$ A cm^{-2}, and $j_{min} = 3.65 \times 10^7$ A cm^{-2} for the Ta-Pt-capped oblique sputtering SAF.

Figures 5(c) and 5(d) show the velocity of DW1 and DW2, the DW velocity difference Δv, and the relative ratio of velocity difference η between DW1 and DW2 in the oblique sputtering SAFs. Here, $H_L^{DM} = -1175$ Oe, $H_U^{DM} = 400$ Oe, $H_L^{DLy} = 200$ Oe (corresponding to current density $j_L = 6.76 \times 10^7$ A cm^{-2}), $H_U^{DLy} = 100$ Oe, $H_L^{FLz} = 10$ Oe, and $H_U^{FLz} = 15$ Oe are used. In Fig. 5(d), the relative ratio of velocity difference $\eta > 1\%$ at $H_x = 0$ indicates a field-free magnetization switching, and $\Delta v = 0$ ($\eta = 0$) at $H_x = -1077$, -74, and 1750 Oe indicates no magnetization switching near these three magnetic fields. This is in very good agreement with the experimental observation in Fig. 5(b). Figure 5(e) gives the calculated azimuth angles (ψ_L^1, ψ_U^1) of DW1 and (ψ_L^2, ψ_U^2) of DW2 as a function of H_x for oblique sputtering SAFs. It can be seen that, at $H_x = 0$ ($\psi_L^1 = 148°$, $\psi_U^1 = -53°$, $\psi_L^2 = 33°$, and $\psi_U^2 = 232°$), the symmetry of DW1 (ψ_L^1, ψ_U^1) about the y axis, the symmetry of DW2 (ψ_L^2, ψ_U^2) about the y axis, and the symmetry of DW1 and DW2 about the y axis are simultaneously broken. In this case, DW1 and DW2 have different DW velocities, and thus, the field-free magnetization switching occurs without the external magnetic field.

From the above, although the Pt-Ta-, Ta-Ru-, and Ta-Pt-capped SAF films have quite different physical parameters such as K^p, J^{ex}, H^{DM}, and H^{DLy}, we can see that the relative ratio of velocity difference $\eta = 1\%$ as the theoretical criterion to define the critical field H^{crit} can perfectly describe all the experimental critical field of various SAF films. It is well known that, when the magnetization switching is caused by the external magnetic field through DW movement, the critical field should overcome the pinning magnetic field on the DWs. On the other hand, the chiral DWs can also be moved by pure electric current without the external magnetic field [2], which can define a critical electric current to produce the SOT effective field to overcome the pinning magnetic field and move the DWs. However, the conventional SOT effective field can only make the two chiral DWs move with the same velocity (i.e., the two chiral DWs still degenerate) and cannot determinate perpendicular magnetization switching. There-

fore, in the case of enough big applied electric currents, the defined critical field H^{crit} by $\eta = 1\%$ is not the depinning field but a critical field to break the degeneracy of moving chiral DWs to switch the perpendicular magnetization. In this sense, our definition of the critical field is universally applicable to other magnetic materials where the magnetization switching is caused by DW movement.

Finally, let us discuss the relation between the critical magnetic field and interfacial DMI and SOT in SAFs. The DW dynamical calculations indicate that the low field magnetization switching in the Pt-Ta-capped SAF is due to the weak DMI ($H_U^{DM} = 500$ Oe) in the UM despite the large IAC ($H^{ex} = 6724$ Oe) and large DMI ($H_L^{DM} = -1625$ Oe) in the LM. On the contrary, the high critical field for magnetization switching in the Ta-Ru-capped SAF is caused by the large DM interaction ($H_L^{DM} = -3600$ Oe and $H_U^{DM} = 3600$ Oe) in both magnetic layers and strong IAC ($H^{ex} = 3137$ Oe) between both magnetic layers. Moreover, in addition to the quite different DMIs at bottom and top interfaces, the fieldlike effective magnetic fields along the z axis ($H_L^{FLz} = 10$ Oe and $H_U^{FLz} = 15$ Oe) greatly enhance the field-free SOT-induced perpendicular magnetization switching in the oblique sputtering SAFs. It is worth mentioning that the fieldlike effective magnetic fields (H_L^{FLz} and H_U^{FLz}) acted on DW1 and DW2 are the same, so they can serve as the bias magnetic fields to switch the perpendicular magnetization. By contrast, for dampinglike SOT effective field $\mathbf{H}^{DLy}$, its direction is determined by $-\mathbf{M} \times \mathbf{p}$, where $\mathbf{p}$ represents the spin polarization of spin current from the spin Hall effect. If there is no external magnetic field, the corresponding $\mathbf{H}_L^{DLy}$ and $\mathbf{H}_U^{DLy}$ in DW1 show opposite signs as compared with those in DW2. Therefore, the fieldlike effective magnetic fields $\mathbf{H}_L^{FLz}$ and $\mathbf{H}_U^{FLz}$ are more efficient than the dampinglike effective field $\mathbf{H}_L^{DLy}$ and $\mathbf{H}_U^{DLy}$ for the field-free SOT-induced perpendicular magnetization switching in strong coupling SAFs.

VI. CONCLUSIONS

In conclusion, by modulating the interfacial DMI and SOT of bottom and top interfaces, the critical magnetic field for the SOT-induced magnetization switching can be varied in a wide range from field free to 3000 Oe in perpendicularly magnetized CoPt/Ru/CoPt SAFs with strong IAC. These findings provide key insights for understanding the role of DMI and SOT in magnetization switching of magnetically coupled chiral systems and pave the way to practical applications of high-performance and low-power-consumption spintronic devices based on SAFs.

[1] R. A. Duine, K.-J. Lee, S. S. P. Parkin, and M. D. Stiles, Synthetic antiferromagnetic spintronics, Nat. Phys. **14**, 217 (2018).

[2] S.-H. Yang, K.-S. Ryu, and S. Parkin, Domain-wall velocities of up to $750 \, \mathrm{m \, s^{-1}}$ driven by exchange-coupling torque in synthetic antiferromagnets, Nat. Nanotechnol. **10**, 221 (2015).

[3] A. Fernández-Pacheco, E. Vedmedenko, F. Ummelen, R. Mansell, D. Petit, and R. P. Cowburn, Symmetry-breaking interlayer Dzyaloshinskii-Moriya interactions in synthetic antiferromagnets, Nat. Mater. **18**, 679 (2019).

[4] D.-S. Han, K. Lee, J.-P. Hanke, Y. Mokrousov, K.-W. Kim, W. Yoo, Y. L. W. van Hees, T.-W. Kim, R. Lavrijsen, C.-Y. You, H. J. M. Swagten, M.-H. Jung, and M. Kläui, Long-range chiral exchange interaction in synthetic antiferromagnets, Nat. Mater. **18**, 703 (2019).

[5] C. Bi, H. Almasi, K. Price, T. Newhouse-Illige, M. Xu, S. R. Allen, X. Fan, and W. Wang, Anomalous spin-orbit torque switching in synthetic antiferromagnets, Phys. Rev. B **95**, 104434 (2017).

[6] G. Y. Shi, C. H. Wan, Y. S. Chang, F. Li, X. J. Zhou, P. X. Zhang, J. W. Cai, X. F. Han, F. Pan, and C. Song, Spin-orbit torque in MgO/CoFeB/Ta/CoFeB/MgO symmetric structure with interlayer antiferromagnetic coupling, Phys. Rev. B **95**, 104435 (2017).

[7] P. X. Zhang, L. Y. Liao, G. Y. Shi, R. Q. Zhang, H. Q. Wu, Y. Y. Wang, F. Pan, and C. Song, Spin-orbit torque in a completely compensated synthetic antiferromagnet, Phys. Rev. B **97**, 214403 (2018).

[8] M. Belmeguenai, H. Bouloussa, Y. Roussigné, M. S. Gabor, T. Petrisor, C. Tiusan, H. Yang, A. Stashkevich, and S. M. Chérif, Interface Dzyaloshinskii-Moriya interaction in the interlayer antiferromagnetic-exchange coupled Pt/CoFeB/Ru/CoFeB systems, Phys. Rev. B **96**, 144402 (2017).

[9] A. Hrabec, Z. Luo, L. J. Heyderman, and P. Gambardella, Synthetic chiral magnets promoted by the Dzyaloshinskii-Moriya interaction, Appl. Phys. Lett. **117**, 130503 (2020).

[10] A. Manchon, J. Železný, I. M. Miron, T. Jungwirth, J. Sinova, A. Thiaville, K. Garello, and P. Gambardella, Current-induced spin-orbit torques in ferromagnetic and antiferromagnetic systems, Rev. Mod. Phys. **91**, 035004 (2019).

[11] J. Ryu, S. Lee, K.-J. Lee, and B.-G. Park, Current-induced spin-orbit torques for spintronic applications, Adv. Mater. **32**, 1907148 (2020).

[12] M. N. Baibich, J. M. Broto, A. Fert, F. Nguyen Van Dau, F. Petroff, P. Etienne, G. Creuzet, A. Friederich, and J. Chazelas, Giant Magnetoresistance of (001)Fe/(001)Cr Magnetic Superlattices, Phys. Rev. Lett. **61**, 2472 (1988).

[13] S. S. P. Parkin, N. More, and K. P. Roche, Oscillations in Exchange Coupling and Magnetoresistance in Metallic Superlattice Structures: Co/Ru, Co/Cr, and Fe/Cr, Phys. Rev. Lett. **64**, 2304 (1990).

[14] X. Zhang, Y. Zhou, and M. Ezawa, Magnetic bilayer-skyrmions without skyrmion Hall effect, Nat. Commun. **7**, 10293 (2016).

[15] S. H. Skjærvø, C. H. Marrows, R. L. Stamps, and L. J. Heyderman, Advances in artificial spin ice, Nat. Rev. Phys. **2**, 13 (2020).

[16] J. Lan, W. Yu, and J. Xiao, Antiferromagnetic domain wall as spin wave polarizer and retarder, Nat. Commun. **8**, 178 (2017).

[17] R. Chen, Q. Cui, L. Liao, Y. Zhu, R. Zhang, H. Bai, Y. Zhou, G. Xing, F. Pan, H. Yang, and C. Song, Reducing Dzyaloshinskii-Moriya interaction and field-free spin-orbit torque switching in synthetic antiferromagnets, Nat. Commun. **12**, 3113 (2021).

[18] X. Wang, C. Wan, W. Kong, X. Zhang, Y. Xing, C. Fang, B. Tao, W. Yang, L. Huang, H. Wu, M. Irfan, and X. Han, Field-free programmable spin logics via chirality-reversible spin-orbit torque switching, Adv. Mater. **30**, 1801318 (2018).

[19] X. Xie, X. Zhao, Y. Dong, X. Qu, K. Zheng, X. Han, X. Han, Y. Fan, L. Bai, Y. Chen, Y. Dai, Y. Tian, and S. Yan, Controllable field-free switching of perpendicular magnetization through bulk spin-orbit torque in symmetry-broken ferromagnetic films, Nat. Commun. **12**, 2473 (2021).

[20] S. H. Yang, C. Garg, and S. S. P. Parkin, Chiral exchange drag and chirality oscillations in synthetic antiferromagnets, Nat. Phys. **15**, 543 (2019).

[21] D. MacNeill, G. M. Stiehl, M. H. D. Guimaraes, R. A. Buhrman, J. Park, and D. C. Ralph, Control of spin-orbit torques through crystal symmetry in WTe$_2$/ferromagnet bilayers, Nat. Phys. **13**, 300 (2017).

[22] G. Yu, P. Upadhyaya, Y. Fan, J. G. Alzate, W. Jiang, K. L. Wong, S. Takei, S. A. Bender, L.-T. Chang, Y. Jiang *et al.*, Switching of perpendicular magnetization by spin-orbit torques in the absence of external magnetic fields, Nat. Nanotechnol. **9**, 548 (2014).

[23] Y. Cao, Y. Sheng, K. W. Edmonds, Y. Ji, H. Zheng, and K. Wang, Deterministic magnetization switching using lateral spin-orbit torque, Adv. Mater. **32**, 1907929 (2020).

[24] L. Liu, C. Zhou, X. Shu, C. Li, T. Zhao, W. Lin, J. Deng, Q. Xie, S. Chen, J. Zhou *et al.*, Symmetry-dependent field-free switching of perpendicular magnetization, Nat. Nanotechnol. **16**, 277 (2021).

[25] H. Wu, J. Nance, S. A. Razavi, D. Lujan, B. Dai, Y. Liu, H. He, B. Cui, D. Wu, K. Wong *et al.*, Chiral symmetry breaking for deterministic switching of perpendicular magnetization by spin-orbit torque, Nano Lett. **21**, 515 (2021).

[26] Q. Ma, Y. Li, D. B. Gopman, Y. P. Kabanov, R. D. Shull, and C. L. Chien, Switching a Perpendicular Ferromagnetic Layer by Competing Spin Currents, Phys. Rev. Lett. **120**, 117703 (2018).

[27] J. Torrejon, J. Kim, J. Sinha, S. Mitani, M. Hayashi, M. Yamanouchi, and H. Ohno, Interface control of the magnetic chirality in CoFeB/MgO heterostructures with heavy-metal underlayers, Nat. Commun. **5**, 4655 (2014).

[28] A. Soumyanarayanan, M. Raju, A. L. Gonzalez Oyarce, A. K. C. Tan, M.-Y. Im, A. P. Petrović, P. Ho, K. H. Khoo, M. Tran, C. K. Gan, F. Ernult, and C. Panagopoulos, Tunable room-temperature magnetic skyrmions in Ir/Fe/Co/Pt multilayers, Nat. Mater. **16**, 898 (2017).

[29] G. Chen, T. Ma, A. T. N'Diaye, H. Kwon, C. Won, Y. Wu, and A. K. Schmid, Tailoring the chirality of magnetic domain walls by interface engineering, Nat. Commun. **4**, 2671 (2013).

[30] F. Meier, S. Lounis, J. Wiebe, L. Zhou, S. Heers, P. Mavropoulos, P. H. Dederichs, S. Blügel, and R. Wiesendanger, Spin polarization of platinum (111) induced by the proximity to cobalt nanostripes, Phys. Rev. B **83**, 075407 (2011).

[31] See Supplemental Material at http://link.aps.org/supplemental/10.1103/PhysRevB.105.144434 for details of more experimental results and theoretical calculations.

[32] S. Zhang and Z. Li, Roles of Nonequilibrium Conduction Electrons on the Magnetization Dynamics of Ferromagnets, Phys. Rev. Lett. **93**, 127204 (2004).

[33] A. Thiaville, Y. Nakatani, J. Miltat, and Y. Suzuki, Micromagnetic understanding of current-driven domain wall motion in patterned nanowires, Europhys. Lett. **69**, 990 (2005).

[34] A. P. Malozemoff and J. C. Slonczewski, *Magnetic Domain Walls in Bubble Materials* (Academic Press, New York, 1979).